Automated fiber coupling and probe beam characterization for Rydberg excitation

Dominik Wawrzinek

Bachelorarbeit in Physik
angefertigt im Institut für Angewandte Physik

vorgelegt der
Mathematisch-Naturwissenschaftlichen Fakultät
der
Rheinischen Friedrich-Wilhelms-Universität
Bonn

August 2026

Ich versichere, dass ich diese Arbeit selbstständig verfasst und keine anderen als die angegebenen Quellen und Hilfsmittel benutzt sowie die Zitate kenntlich gemacht habe.

Bonn, ...

Datum Unterschrift

Gutachter und Betreuer: Prof. Dr. Sebastian Hofferberth
Gutachter: Prof. Dr. Daqing Wang

Acknowledgements

I would like to thank everyone who supported me over the course of this bachelor's thesis. Starting with Sebastian Hofferberth, thank you for giving me the opportunity to be part of this amazing research group, for trusting in me and for guiding me throughout this thesis. Thank you Daqing Wang for being my second supervisor and thank you Wolfgang Alt for your thought-provoking impulses.

A special thank you goes to all the HQO members including Julia, Darius, Valerie, Alican, Theresa and Teresa for all the fun tea breaks, for answering all of my questions and for being just wonderful people to work and spend time with. A big thank you goes to Darius and Julia for the quick proofreading of my thesis, I did not make it easy for you guys. And of course all the thanks to you Julia for being my supervisor, for your support before, during and after this thesis and for literally always being available to answer questions. Also thank you to all the other members of the NQO group for being such a nice bunch of people.

I would also like to thank all my friends at university, I would not have made it this far without you guys and gals. Finally, I would like to thank my parents for their endless support.

Contents

CHAPTER 1

Introduction

Physical platforms for quantum technologies have seen a rapid increase of interest in recent years as they promise novel possibilities for domains such as metrology [1] and cryptography [2] while also giving rise to completely new fields like quantum computing [3]. Two promising platforms for example include superconducting circuits as well as neutral atom ensembles, each with different advantages. In order to benefit from their respective advantages, hybrid systems are being developed to interface these platforms [4].

The Hybrid Quantum Optics (HQO) experiment in the Nonlinear Quantum Optics group led by Sebastian Hofferberth investigates a hybrid system between an electromechanical oscillator and Rubidium Rydberg atoms [5]. One goal of the experiment is to cool an oscillator mode into its ground state by extracting phonons via interaction with the Rydberg atoms [6]. To minimize thermal occupation of the oscillator modes, the experiment is planned to be conducted in a 4 K environment inside a cryostat.

To excite the Rydberg atoms required for this hybrid system, a two-photon excitation scheme for ^{87}Rb is used, where a 780 nm laser excites the Rubidium to an intermediate state while a 480 nm laser is used to excite to the Rydberg state from there. With the arrival of the cryostat, it is planned to focus the laser beams used for Rydberg excitation such that the beam waist at the focus is larger than the blockade radius [7] to allow for the excitation of multiple Rydberg atoms which can then interact with the oscillator. To detect whether Rydberg excitations were induced, single photon counters are used to collect the 780 nm light traversing the trapped Rubidium cloud, which enables to check for example for electromagnetically induced transparency [8] or Autler-Townes splitting [9].

A reliable single-photon detection is therefore an essential technical component of the HQO experiment, providing access to photon statistics, correlations, and nonlinear optical response. However, factors such as thermal fluctuation and vibrations can cause misalignment, which reduces the fraction of transmitted power and necessitates realignment. Frequent manual realignment can be time consuming, which motivates the development of a fast and effective system for automated fiber coupling. Previous work on automated fiber coupling has demonstrated the feasibility of using optimization algorithms such as Bayesian optimization and differential evolution to align laser beams via actuated mirrors [10]. Therefore, a system was developed over the course of this thesis which uses mirror mounts with piezoelectric actuators in combination with a machine-learning based optimization algorithm known as M-LOOP [11].

The thesis is structured as follows. Chapter 2 presents the automated fiber coupling system by first illustrating the concept of fiber coupling and introducing the piezoelectric actuators used for this project. Based on this, the optimization algorithm is outlined and its performance in different setups reviewed. In

Chapter 3 the optical setup for Rydberg excitation is presented in order to outline the characterization of the 780 nm beam in the setup. The chapter concludes with a performance review of the optical setup after introducing the components characterized in this thesis.

CHAPTER 2

Automatic fiber coupling optimization

Efficiently coupling light from free space into an optical fiber is essential for many AMO experiments, where fibers are commonly used to guide laser light between different parts of the setup. The kinematic mirror mounts which are usually used to align laser light with a fiber have to be adjusted by hand, and while careful manual adjustment can achieve sufficiently high coupling efficiencies, environmental influences such as temperature changes or vibrations gradually shift the alignment over time.

Restoring optimal coupling then requires frequent manual readjustment, which becomes especially impractical when mirror mounts are difficult to access or when many fiber couplings need to be maintained simultaneously. Replacing these mounts with piezoelectric actuators addresses this problem, as it enables the mirrors to be repositioned automatically and precisely via computer control. A goal of this thesis is to create a system for the optical setup for Rydberg excitation of the HQO experiment that utilizes this capability.

This chapter is structured as follows. Section 2.1 covers the theoretical background needed to understand the alignment techniques discussed later. Section 2.2 introduces the piezoelectric actuators used to steer the mirrors and presents a characterization of their movement, which is a prerequisite for controlling them reliably. Building on this characterization, Section 2.3 presents the machine-learning-based setup developed to automate the fiber coupling process.

2.1 Theoretical background of fiber coupling

Fiber coupling describes the process of guiding a laser beam from free space into an optical fiber. In order to maximize the fraction of power transmitted, called the coupling efficiency, the incoming laser light needs to enter the fiber in the correct angle for total internal reflection to occur while simultaneously having as much overlap as possible with the fiber core (total internal reflection can occur if the refractive index of the fiber core is larger than that of the surrounding cladding, the light is for the most part then trapped inside the fiber core until escaping at the other end of the fiber [12]). This is typically achieved using two beam steering mirrors in succession, for example as in Fig. 2.1, which depicts a simple fiber coupling setup that was also used for many of the measurements later on.

The kinematic mirror mounts generally used for this possess two screws which can respectively alter the mirrors pitch θ and yaw ϕ. With two mirror mounts this results in four degrees of freedom for the beam, two for the placement of the beam on the two dimensional surface of the fiber and two for entering the fibers core in the correct angle.

Figure 2.1: Sketch of a simple fiber coupling setup with four labeled angular displacements of the mirrors. The pitch angles are θ_1 and θ_2, and the yaw angles are ϕ_1 and ϕ_2. The mirrors guide the input beam towards the focussing lens, which focuses the beam to the size of the fiber core in order to collect the laser light with the fiber. Image modified from [13].

The focussing lens in front of the fiber in Fig. 2.1 focuses the beam to the size of the fiber core so as to collect all of the laser beams light. Fig. 2.2 shows how one can then imagine the interplay of a mirrors angle and the position of the beam on a surface at the focal length of the focussing lens using the simplified ray optics model. It is then possible to calculate the relation between the mirror tilt θ and the displacement d on a surface via the equation [14]

$$\theta = \frac{\arctan(d/f)}{2} \approx \frac{d}{2f} \quad \Leftrightarrow \quad d \approx \theta \cdot 2f. \tag{2.1}$$

For mirror mount systems which perform quantized movements, like ones with piezoelectric actuators, both θ and d are then also quantized, being then called the step size of the system and given either as angle θ or covered distance of the beam d.

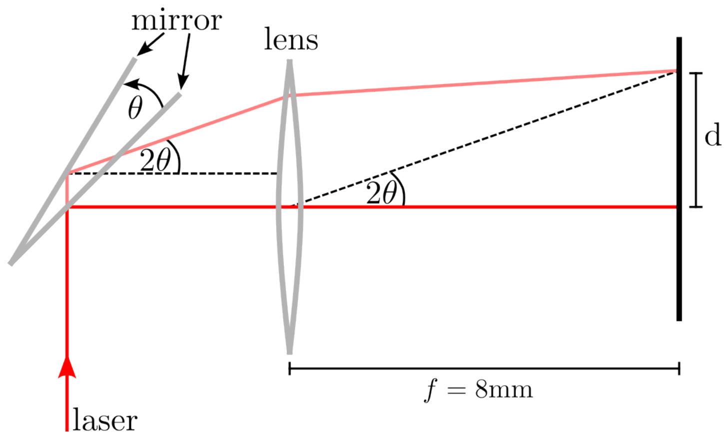

Figure 2.2: Simplified depiction of a laser beam's path in a fiber coupling setup before (dark red) and after (light red) tilting a mirror. The dotted lines are support lines that show how the relation between the mirror tilt θ and distance d can be calculated via Eq. 2.1. The surface on which d sits has to be at the focal distance f of the lens for this to hold true. Image adapted from [14].

The optical fiber the light is being coupled into is the Thorlabs P3-780PM-FC, a single mode fiber whose core diameter is slightly smaller than its mode field diameter given as (5.3 ± 0.1) µm [15]. The mode field diameter describes the extend to where the beam's intensity is above $1/e^2$ of its maximum intensity. To understand this, it has to mentioned that the ray optics model used for describing a laser beam is only a simplification, a more accurate model which is used when light interacts with structures whose size is roughly of the same order as its wavelength is that of a Gaussian beam whose amplitude envelope in the transverse plane is given by a Gaussian function. The single mode fiber ensures that only this fundamental transverse mode is being transmitted, more information on this can be taken from [12]. Another quantity that becomes important later on in Chapter 3 is the beam waist, the radius at which the amplitude of a Gaussian beam is $1/e$ of its maximum value at the same axial position.

Fig. 2.3 depicts a not to scale sketch of the fibers surface, showing the refractive indices of the core n_1 and the surrounding cladding n_2, which need to satisfy the condition $n_1 > n_2$ to allow for total internal reflection inside the core. The core diameter described above is also shown as well as the distance d which is also featured in Fig. 2.2.

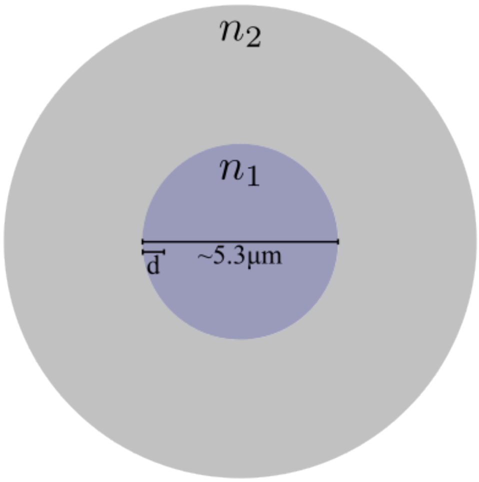

Figure 2.3: Sketch of an optical fiber's core and surrounding cladding. The refractive index of the core n_1 has to be larger than that of the cladding n_2 in order to allow for total internal reflection inside the core. The core diameter is slightly smaller than the mode field diameter given as (5.3 ± 0.1) µm [15]. d shows an arbitrary distance a laser beam moves because of a mirror tilt as shown in Fig. 2.2.

2.2 PiezoMike Linear Actuators

The PiezoMike Linear Actuators by Physik Instrumente [16] have previously been used in the group by E. Huland in his bachelor thesis [14] who characterized their movement and stability for application in an optical dipole trap of the Rubidium Quantum Optics-project (RQO) [17]. As they exhibited suitable properties in his application of precisely aligning two laser beams at the correct position, we decided to use them for our project as well.

Section 2.2.1 explains how the actuators operate and highlights some of their specifications. Section 2.2.2 summarizes the findings of E. Huland regarding the properties of the actuators and displays additional measurements that were done to characterize and optimize the movement of the mirrors.

2.2.1 Working principle and specifications

The actuators are effectively an upgrade to the usual mirror mounts used in most optics lab. The fine threaded screws of the linear actuators run through the wide threaded screws of the mirror mount which enables to adjust them the same way one used to with ordinary mirror mounts, just with enhanced precision because of their small step size, which can for now be understood as the angular tilt of the mirror caused by the smallest movement the linear actuator can produce.

The actuator itself works as follows: when a forward movement command is issued, the actuator receives a sawtooth signal for each step it's supposed to perform. Due to the voltage a piezoelectric crystal (see Fig. 2.4, also called piezo actuator there) expands, which causes the claw it is connected to to rotate the fine threaded screw counter-clockwise. At the end of one such sawtooth, when the voltage drops to zero, the crystal quickly contracts, which causes the claw to slip back into its initial position without turning the screw, this is called the slip stick principle.

The same principle applies for backward movement where the screw is rotated clockwise, here the actuator receives a reverse sawtooth signal which causes the crystal to first contract relatively slow and then expand quickly.

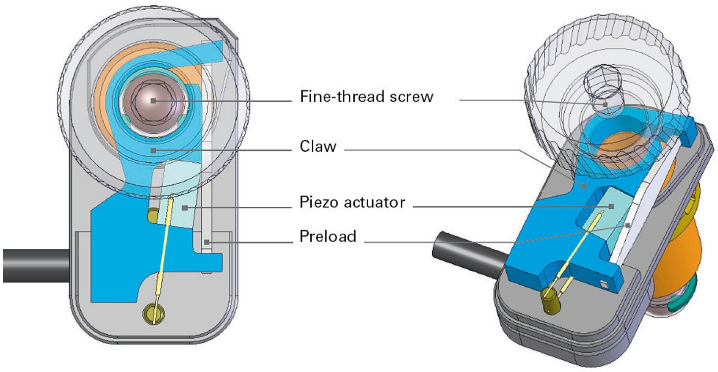

Figure 2.4: Inner workings of the PiezoMike Linear Actuator. When an electric sawtooth signal is applied the piezo actuator expands, which causes the claw to rotate the fine thread screw. After the signal reaches its maximum and quickly drops to zero, the piezo actuator quickly contracts and the claw slips back into its initial position without turning the screw. The preload sets the friction threshold between these two behaviours by pressing the claw against the fine thread screw. Image taken from [16].

The actuator receives the sawtooth signals from a control unit, the E-870.4G PIShift Drive Electronics by Physik Instrumente [18], which is in turn connected to a standard desktop computer and can be issued commands via Python (using the PIPython [19] package) or it's own GUI. Up to four actuators can be connected to the controller, but only one of them receives a signal at any time.

The standard operating voltage is 80 V at a standard operating frequency of 400 Hz [20]. Since each step corresponds to one full sawtooth cycle, the frequency of the applied signal directly determines the speed of the mirror movement, the actuator can therefore perform up to 400 steps per second. The lifetime of the actuators is given as 1 billion steps, with an expected decrease of the step size by a maximum of 30 % [16]. The long lifetime ensures that step size degradation is not a practical concern within the scope of this thesis, but for the future implementation in the experiment its impact needs to be observed.

2.2.2 Characterization of actuator movement

It is important to characterize the actuator movement before being able to perform automated fiber coupling to make sure the relationship between an issued move command and the actual movement of the mirror is linear and reproducible. Otherwise the optimization algorithm would struggle to accurately target a specific mirror position, making the automation unreliable. The same actuators used in this thesis were already partially characterized by E. Huland in his bachelor thesis [14] and found to have properties suitable for our application.

His results could therefore be used as a basis for the automated optimization, so that his values could be adapted for the specific application at hand rather than new measurements having to be performed from scratch. In the following, E. Huland's findings are first summarized, and the measurements performed to convert and fine-tune his values for use in the fiber coupling algorithm are then described.

In his thesis, E. Huland conducted multiple measurements regarding the step sizes of each actuator and the stability of the mirror mounts. In particular, he discovered that

- the actuators behave linearly, meaning the step sizes don't vary across their movement range.
- each actuator has a different step size, likely due to prior wear and manufacturing tolerances. The step sizes measured are given as b_{fw} and b_{bw} in (see Table 2.1) in units of µrad because he measured them as angular tilt of the mirror.
- the mirror mounts showed a small drift in their angular position over the course of 20 hours after being freshly installed in an optical setup, but after this period of time the drift leveled out.

In conclusion, the mirror mounts with linear actuators can be reliably controlled due to their linear behaviour and after a settle time of about 1 day they show little to no drift in their pointing stability. But, the difference in step size for each actuator and each direction needs to be considered, as they vary by up to ~ 31 % in forward direction and ~ 24 % in backward direction as can be seen in Table 2.1.

Serial number	b_{fw} / µrad	b_{bw} / µrad
114048213	0.81 ± 0.05	0.74 ± 0.04
114048208	0.53 ± 0.03	0.54 ± 0.03
114048215	0.71 ± 0.04	0.65 ± 0.04
114048206	0.56 ± 0.03	0.56 ± 0.03

Table 2.1: By E. Huland [14] measured step sizes b_{fw} and b_{bw} in forward and backward direction as angular displacement of the mirrors.

As explained at the start of Section 2.1 it is important to be able to steer a laser beam reliably in order to maximize the amount of transmitted power from free space into an optical fiber. To investigate how the difference in forward and backward step size of the actuators (see Table 2.1) impacts the ability to steer the beam into a position and then back, a Python script was used which does this forward and backward movement for multiple iterations and measures the detected laser power after each movement using a power meter. A sketch of the setup used can be seen in Fig. 2.5. It includes an out- and an incoupler (respectively with a $f = 8$ mm focussing lens), two mirror mounts with linear actuators and a PM100USB power meter [21] connected to the fiber of the incoupler.

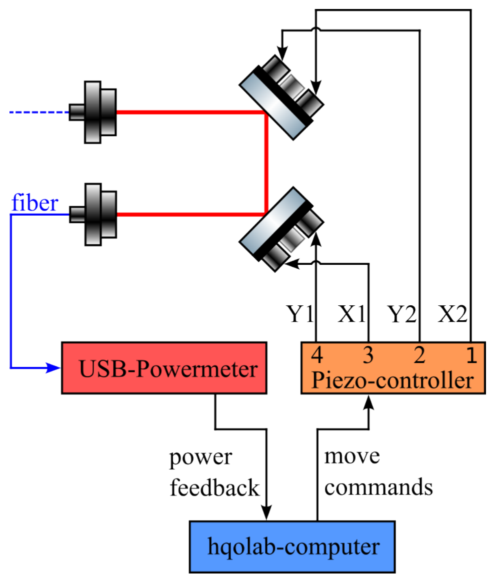

Figure 2.5: Sketch of the setup used for the movement characterization measurements and tests of the optimization algorithm. The laser beam enters the optical setup through the outcoupler from the top left and is steered into the incoupler by the two mirrors with linear actuators. The measured power of the PM100USB power meter [21] can be read out by a computer and used as feedback to move the mirrors into a more optimal position.

The script takes a certain distance D that the beam should move across the optical fibers surface (analogous to d in Fig. 2.2 & 2.3) as an argument and calculates the required number of steps N to cover the distance via the simple equation

$$N_{\text{fw/bw}} = \frac{D}{d_{\text{fw/bw}}}. \tag{2.2}$$

As can be seen, the equation uses the step size $d_{\text{fw/bw}}$, which is the converted step size from units of µrad to units of nm via Eq. 2.1 with the focal length $f = 8\,\text{mm}$ of the incoupler lens, which not only makes this calculation possible, but also makes the numbers more tangible: as explained in Section 2.1, the optical fibers used for this project have a core diameter of roughly $(5.3 \pm 0.1)\,\mu\text{m}$, so 1 step (assuming $d \approx 10\,\text{nm}$) is only $\sim 0.2\,‰$ of the distance from one end of the fiber core's surface to another, further enhancing the notion that the linear actuators are suitable for precise optical alignment. The calculated step sizes are given in Table. 2.2.

Serial number	d_{fw} / nm	d_{bw} / nm
114048213	12.96 ± 0.80	11.84 ± 0.64
114048208	8.48 ± 0.48	8.64 ± 0.48
114048215	11.36 ± 0.64	10.40 ± 0.64
114048206	8.96 ± 0.48	8.96 ± 0.48

Table 2.2: Step sizes d_{fw} and d_{bw} in forward and backward direction as laser beam displacement on a surface. Calculated from the values in Table 2.1 via equation 2.1.

Fig. 2.6(a) shows one of the movement characterization measurements for channel 1 (each actuator has an assigned channel as can be seen in Table 2.3). The actuator performed as many steps as it was required by Eq. 2.2 for the laser beam to cover a distance of 1 µm on the fiber surface, first in forward direction and afterwards in backward direction. It did this for 50 iterations, taking a power measurement before (labeled Start) and after (Mid) each forward move and one after each backward move (End). After each movement the actuators waited for 0.1 s so the mirror could settle for the power measurement.

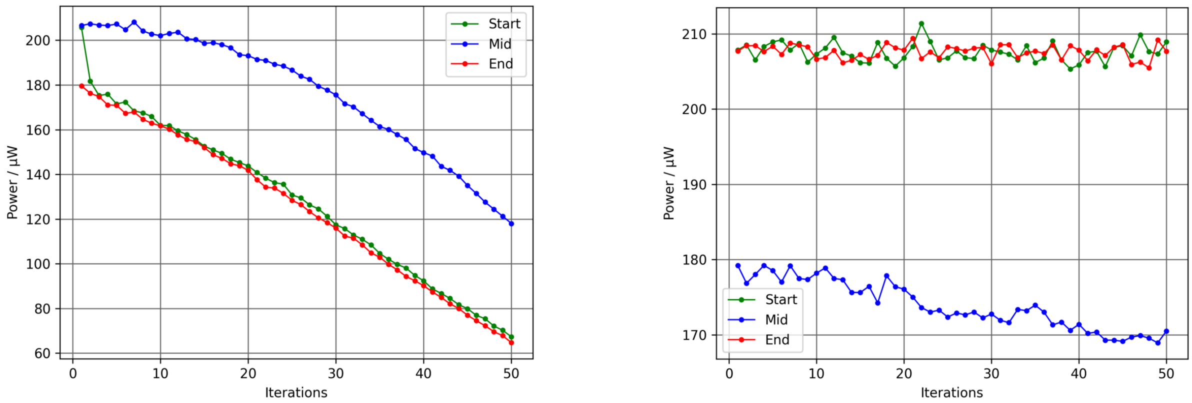

(a)

(b)

Figure 2.6: To match the values of d_{fw} and d_{bw} so that the same distances can reliably be covered for forward and backward movement, alternating backward and forward commands were issued and the power after every step measured to test if the beam was indeed moved back to the same spot as before. This was done over a distance of 1 µm for 50 iterations to see if there is a trend which hints to some discrepancy. **(a)** shows a measurement series before adjusting the step sizes, where a discrepancy is indeed visible as all measured powers decrease over time, while **(b)** shows one after adjusting the backward step size as shown in Table 2.3 until all the power measurements stay (mostly) constant.

As can be seen in Fig. 2.6(a) all power measurements decline over time, even though the laser is moved to a position of better coupling by the 1 µm movement it performs as can be deduced by the Mid power values being higher than the others. The decline can be attributed to a difference in the distance covered for the forward and backward movement, in this case a larger movement in the backward direction, which is the crucial point to understand here:

Initially the measurement series of almost all actuators showed some decline as the step sizes did not lead to the same distance being covered in both directions. By iteratively adjusting the step sizes for backward movement by taking a measurement series and observing how the measured values changed, it was achieved to minimize the difference of the distance covered in both directions as can for example be seen in Fig. 2.6(b) for the channel 2 actuator. This was done for all actuators, the resulting adjusted backward step sizes are denoted in Table 2.3. The step size of the channel 3 actuator did not need to be adjusted. It was not possible to completely remove the decline for all measurements because of the finite length of the step sizes which cannot be chosen arbitrarily small, but sufficiently enough for the movements the optimization algorithm later performs.

It was not measured if these step sizes exactly match the real step sizes performed by the beam as it is not important as long as the same distance is covered for forward and backward movement. It has to be noted that the step sizes can decrease over time as mentioned in Section 2.2.1, so it has to be observed if the step sizes need to be readjusted in the future.

As mentioned before, the fluctuations of consecutive power measurements are to be expected, as they

Serial number	d_{bw} (initial) / nm	d_{bw} (adjusted) / nm	Channel
114048213	11.84 ± 0.80	11.34	1
114048208	8.64 ± 0.48	8.94	2
114048215	10.40 ± 0.64	10.40	3
114048206	8.96 ± 0.48	9.20	4

Table 2.3: Initial and adjusted backward step sizes d_{bw} of each actuator. Some of the backward step sizes have been adjusted to make the beam move the same amount in both directions when issuing a move command. As the adjusted values were chosen and not measured, no error is given. Each actuator was assigned a channel number within the control unit mentioned in Section 2.2.1.

can be attributed to intensity fluctuations of the laser. Fig. 2.7 shows 1000 power measurements over the course of 10 s without any actuator movement in between. The measurements fluctuate by about 2 % from the mean value of ~ 227 µW, which is about the same as for the Start and End measurements in Fig. 2.6.

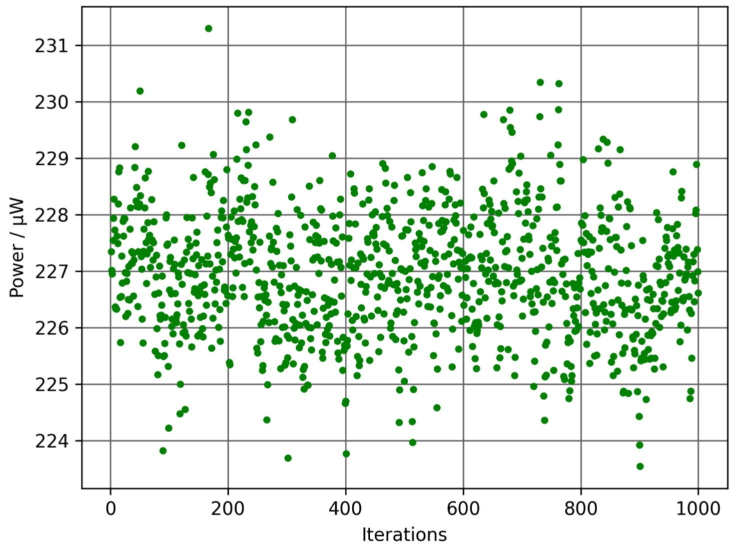

Figure 2.7: To experimentally find the powermeters measurement error, 1000 consecutive power measurements were taken over a span of 10 s without any actuator movement between them. The measurements fluctuate by a maximum amount of about 2 % from the mean value of ~ 227 µW.

With this it can be concluded that it was possible to adjust the backward step sizes of each actuator in order to minimize the discrepancy in forward and backward movement because of the different step sizes in each direction. Fig. 2.6(b) acts as an example of how a movement characterization measurement for each of the actuators has to look like.

2.3 Automated fiber coupling system

Having established that the mirror mounts can be reliably steered by a known amount, the remaining challenge is to find the combination of actuator positions that yields the best possible fiber coupling.

Manually searching this four-dimensional parameter space (two parameters per mirror) can take time, especially if the alignment needs to be repeated regularly or when the setup needs to be altered in order to perform power measurements.

To automate this process M-LOOP [11] was used, a machine-learning optimization package that is well suited for exactly this kind of optimization problem, where the relationship between input parameters and output quality is not known analytically. In the following, Section 2.3.1 explains the working principle of M-LOOP, Section 2.3.2 describes how it was implemented and tested for the application of automatic fiber coupling, and Section 2.3.3 presents its application in the HQO experiment.

2.3.1 M-LOOP optimization algorithm

M-LOOP (Machine-Learning Online Optimization Package) is a Python package developed by P.B. Wigley et al. [11] to automatically and rapidly optimize the parameters of a scientific experiment or computer controlled system. It tries to find the minimum of a cost function, which quantifies the performance of an experiment (in our case the inverse of the laser power as we try to maximize it), by proposing an optimal set of parameters (the mirror positions). To find this optimal set of parameters it uses machine learning to create a model of how the parameters relate to the cost and uses this model to predict parameters that further reduce the cost until an optimum is found, this process is called exploitation. To first create the model and ensure it does not converge on a local minimum, it also proposes parameters in regions of high cost uncertainty, this process is called exploration [22]. The entire approach is known as Bayesian optimization [23].

The package offers five different types of models: Gaussian Process, Neural Net, Differential Evolution, Nelder-Mead and Random, each with different advantages and disadvantages. As the process of optimizing fiber coupling with two mirrors is a computationally undemanding one, the model choice is not as impactful for this application. It was decided to use the Neural Net model, which is a type of model inspired by the biological neurons in brains, in order to understand it better for potential future optimization problems.

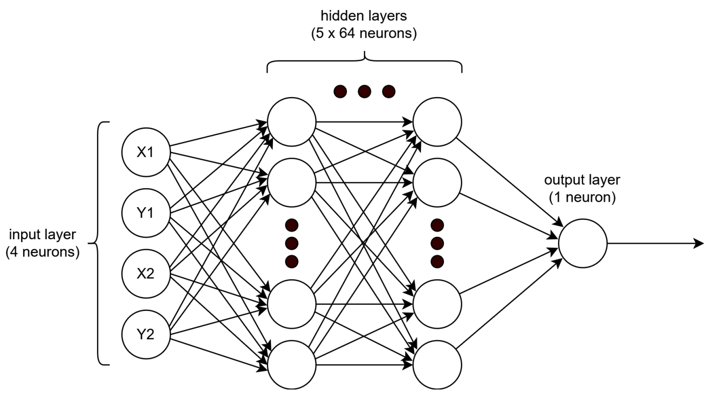

Figure 2.8: Schematic of the neural network implemented in M-LOOP to perform the optimization. The four neurons of the input layer correspond to the four piezo actuators. The neurons of the hidden layers 'process' the input data by calculating a value in each neuron via an activation function $\sigma(z)$ and multiplying it by a weight w. The outputs of the last hidden layer are inserted into the output layer where an output value, the cost, is calculated which can be read out. The image is adapted from an online book [24] which explains neural networks in great detail and simplicity.

Fig. 2.8 shows how the Neural Net model is structured. It consists of four input parameters (input layer), which each correspond to the position of one of the actuators. Each of these parameters is inserted into each of the 64 neurons of the first hidden layer, its name stems from the fact that the user cannot directly interact with it or its output. Each of the neurons contains an activation function, which outputs a float value $\sigma(z)$ depending on the values z inserted into it, just like any other mathematical function. The number of neurons and hidden layers is fixed in the M-LOOP source code [25].

The output of those neurons is then multiplied by a weight w and acts as an input parameter for the neurons of the next hidden layer, which also has 64 neurons which all perform the same computation until, after 5 hidden layers in total, all the outputs of the last hidden layer are inserted into the output neuron, which generates the cost value which can be read out and will then be compared to the real value measured when the input parameters were issued to the actuators.

Depending on how equal the cost value generated by the Neural Net model and the measured value in the experiment are, the weights w of some of the neurons are being adjusted by a small amount Δw until the models output fits the measured value. One can imagine this a bit like fitting a curve to some measured values until the curve touches all of the values or at least their error range. This process is how the model 'learns', hence the words machine learning in the packages name. Fig. 2.9 shows how one can imagine this interplay between the weights of the neural net and its cost.

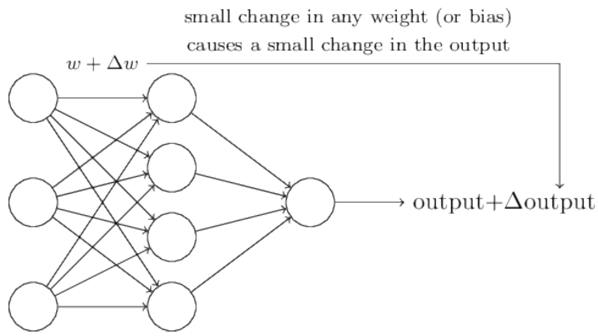

Figure 2.9: Interplay of a neural network's hidden layer and output neurons. In order to match the networks output value with a measured value, the weights w of the neurons in the hidden layers are being adjusted. This process is how the network 'learns'. Image taken from [24].

2.3.2 Experimental setup for testing and characterization

To test if M-LOOP is able to control the actuators and find mirror positions in order to optimize the coupling of a laser into a single-mode fiber, the same setup as for the movement characterization (see Fig. 2.5) is used. Building upon the Python script used for the movement characterization, an additional Python script was created for the optimization algorithm.

As explained in Section 2.2.2, the actuators were not steered by issuing them a specific number of steps they were supposed to perform, but by commanding them to move a certain distance from which the number of required steps is calculated via the fine-tuned step sizes. For the optimization script this methodology was further extended as follows: as mentioned in Section 2.3.1, the parameters given to the Neural Net model refer to the position of each actuator. But the actuators have no means to give feedback on how much their fine threaded screw is turned or something similar from which their position could be deduced.

To solve this issue, the script at first saves its current position as the origin (which is like the origin of our coordinate system from which all positions are defined), with all parameters being zero. If it is then issued a move command to a target position, it saves the parameters of this target position as its new current position. The next time it is supposed to move to a new target position, it first subtracts its current position from the target position and then calculates the required step numbers for each actuator from the leftover distance between the two positions. Otherwise it would would not end up at the right position but rather perform something similar to a random walk, as the target positions are defined relative to the origin and not to the current position.

The centerpiece of the script is in a simplified manner depicted in Fig. 2.10. The M-LOOP initialization function starts the whole process of exploration and exploitation described in Sec. 2.3.1: the script proposes a set of actuator positions which causes the actuators to move their mirrors and at the same time the Neural Net model to generate a cost value with which it predicts the power which will be measured.

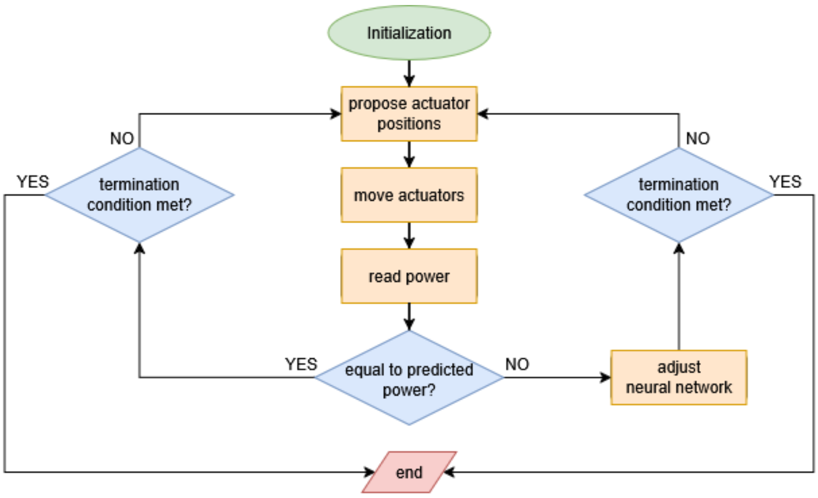

Figure 2.10: Flowchart of the optimization script. After proposing a set of actuator positions, the actuators move into those positions while the Neural Net model generates a cost value. Depending on whether this value and the measured power after the actuator movement match, the neural net is being adjusted to generate the same output value as the actual experiment. This process is repeated until one of the termination conditions for the optimization is met.

If the measured and predicted power values are equal, the script will check if one of the three termination conditions has been met:

1. has the target power been reached? This value can be manually set once one knows what power they want to reach.
2. has the maximum number of runs without any improvement been reached? A run is one loop of the optimization algorithm shown in Fig. 2.10.
3. has the maximum number of runs been reached?

If none of the conditions are met the script proposes a new set of parameters and the cycle starts anew. The third condition almost never comes into action but is helpful for ensuring the script stops at some point.

But as one can imagine, the event of measured and predicted power being not matching and the model therefore not correctly predicting the power is way more likely. In this case, the neural network readjusts the weights of its neuron outputs as described in Section 2.3.1 in order to be able to propose better parameters for the next run.

Fig. 2.11 displays the result of a successful, fully automatic fiber coupling optimization. On the left of the image is a plot showing the evolution of the measured power over the course of 21 runs, so 21 sets of proposed parameters. On the right is an overview with some information about the optimization run and with the parameters that were used. A brief overview of the parameters is given in Appendix A. The displayed parameters provided good results for most optimizations, but can be further tuned once the automated optimization system is introduced into the experiment setup.

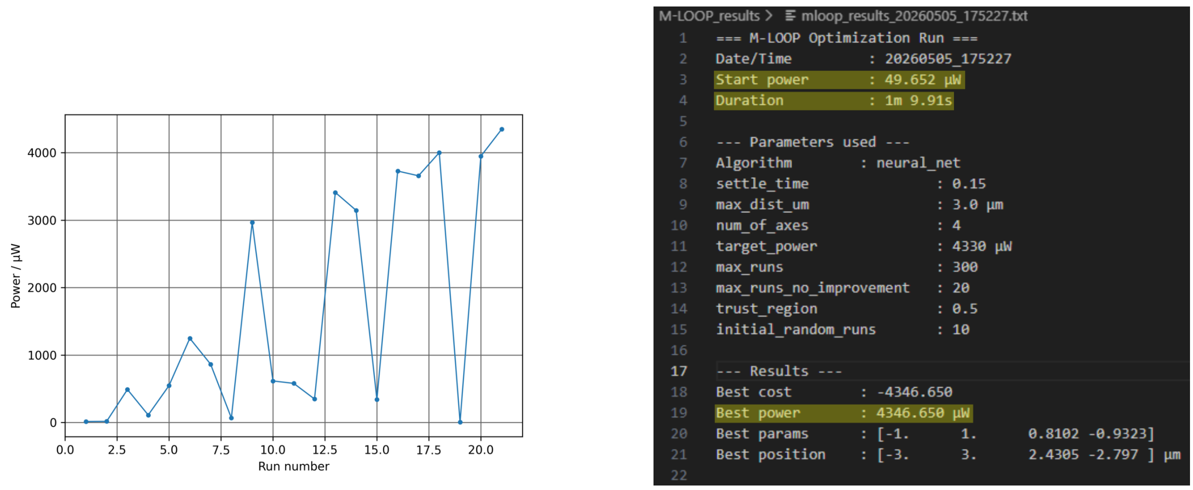

(a) (b)

Figure 2.11: Results of a successful optimization. **(a)** shows the progression of the measured power after each movement to a position proposed by M-LOOP. The valleys stem from runs in which exploration was performed as explained in Section 2.3.1. **(b)** shows a collection of parameters and information about the optimization as the output of the Python code. Highlighted are the start and best power as well as the time the optimization took. The best power is only the highest predicted power by the neural network, the display of the highest measured power was implemented later.

Here one can see for example that the optimization started with about 50 µW of power and stopped at a power of ~ 4 346 µW after ~ 70 s because the target power of 4 330 µW was exceeded. The script achieved this coupling not only faster than most humans could have, but also it only has to be started and can then run on its own. The power of the laser before the incoupler was measured as 5.45 mW which results in a coupling efficiency of ~ 80 %. Other optimizations with higher start powers reached the target power even faster, with durations getting as low as 20 s.

Although the optimization could be performed consistently it has to be noted that for some optimizations which started with a low amount of laser power compared to their achievable maximum, it took a longer time to reach the target power than the run in Fig. 2.11 or they got stuck on a local maximum. Later tests also showed that the optimization works best if the fiber coupling has first been performed by hand and there is still a coupling efficiency of at least ~ 10 % left so that the algorithm only has to realign the mirrors. And as a notice which does not affect the optimization but may be interesting for anyone who wants to implement this system into their setup; the actuators produce a rather obnoxious sound when they move. This could potentially be amended by setting up a sound reducing box around the actuators, which could also improve the temperature stability.

After successfully showing that the automatic fiber coupling with the PiezoMike linear actuators and M-LOOP works, the next section deals with implementing this method in a setup using the count rate of single photon counters as a feedback source instead of a power meter, as this is the setup that will be used in the actual experiment.

2.3.3 Implementation in the experiment

In the actual experiment, the incoupler is connected to a Single Photon Counter Module (SPCM), whose count rate is the new value that that is compared to the cost value of the Neural Net model as the SPCM now replaces the power meter. The SPCM houses four individual single photon counters, but only one is being used for this setup, which is depicted in Fig. 2.12.

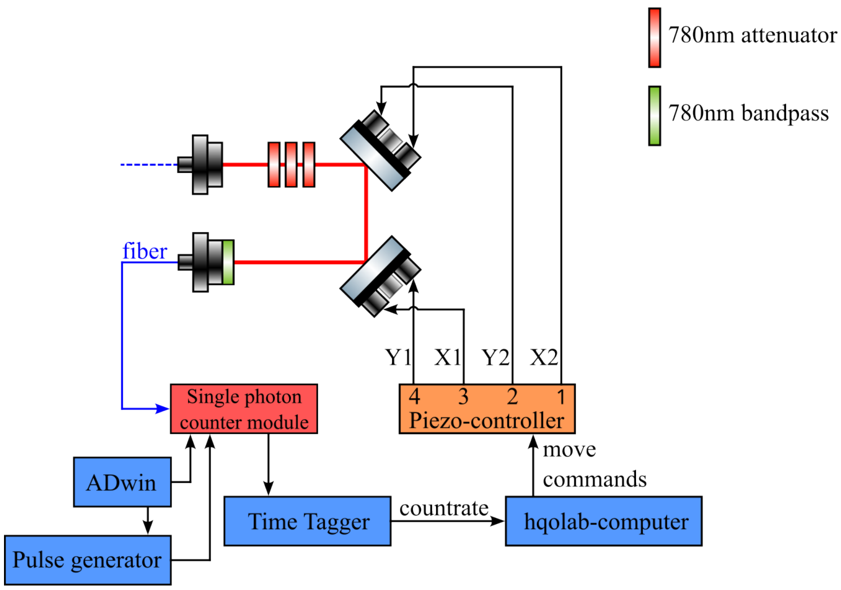

Figure 2.12: Sketch of the setup used for testing the optimization script with SPCM count rates as feedback. The laser beam enters the optical setup through the outcoupler from the top left, is attenuated by three 780 nm attenuators with a combined optical density of 8.62 and is steered into the incoupler by the two mirrors with linear actuators. The incoupler has a 780 nm bandpass filter installed to attenuate other light sources. A single photon counter module is used to detect the amount of photons coupled into the fiber. It receives gate signals from an ADwin-Pro II and a FPGA pulse generator while a Time Tagger 20 read outs the number of detected photons per time frame and provides them as a count rate to a computer.

The SPCs (COUNT-250C-FC from Laser Components) themselves are very fast and sensitive photodiodes (around 45 ns dead time and photon detection efficiency of 50-75% for 780 nm light [26]) whose signals are amplified by a photomultiplier and then counted by a Time Tagger 20 from Swabian instruments, therefore the amount of detected photons in some time frame can be measured as the count rate. The master's thesis of J. Gamper [27] provides more information on the SPCs role in the HQO experiment.

To operate the SPCM which replaces the power meter from before, an ADwin-Pro II and a FPGA pulse generator are added for gate signals. The ADwin-Pro provides many devices with trigger signals through its digital outputs and provides control voltages through its analogue outputs. In this setup it provides both the SPCM and the pulse generator with digital gate signals. More information on this can be found in the bachelor thesis of A. Özcagi [28].

The pulse generator provides the SPCM with four individual gate signals, one for each single photon counter. The gating signals are important as the SPCs can get damaged if the count rate exceeds 20 MHz [26], this is also the reason for the three absorptive neutral density filters with a combined OD (optical density) of 8.62 which attenuate the 780 nm laser beams power and the 780 nm bandpass filter to attenuate stray light.

The optimization algorithm still operates as described in Section 2.3.2, except that it now uses the SPCM count rate as feedback on how good the coupling is rather than the laser power. Fig. 2.13 shows the result of a successful optimization. The plot on the left shows the progression of the measured count rate against the run number while the image on the right gives an overview of the parameters and results of the optimization.

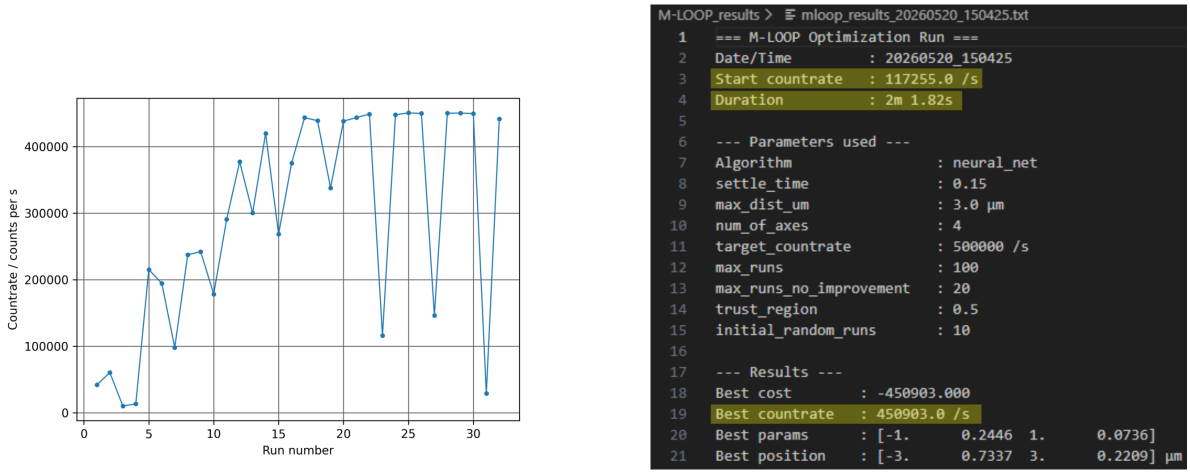

(a) (b)

Figure 2.13: Results of a successful optimization run. **(a)** shows the progression of the measured count rate after each movement to a position proposed by M-LOOP. The valleys stem from runs in which exploration was performed as explained in Section 2.3.1. **(b)** shows a collection of parameters and information about the optimization as the output of the Python code. Highlighted are the start and best count rate as well as the time the optimization took. The best count rate is only the highest predicted count rate by the neural network, the display of the highest measured count rate was implemented later.

The optimization was successful as the count rate was increased from about 117 255 counts/s to 450 983 counts/s in a matter of $\sim$ 122 s. In the case of this optimization the target count rate was set too high, so the optimization went on even though no further improvements were made and was manually stopped. With a fitting target count rate, the optimization is assumed to be 1 minute faster. No coupling efficiency can be given as the count rate before the SPCM could not be measured, but it was not possible to improve the coupling further by hand, leading to the assumption that the best possible coupling was reached.

To conclude, this chapter addressed the motivation outlined at the beginning: replacing the time-consuming manual alignment of mirror mounts with an automated, script-controlled process. By characterizing and fine-tuning the step sizes of the PiezoMike linear actuators (Section 2.2.2), a reliable foundation was established for precisely controlling the mirror positions.

On top of this, the M-LOOP optimization algorithm (Section 2.3) was shown to successfully and quickly optimize the fiber coupling, both with a power meter and on a single photon level with a SPCM setup also used in the actual experiment. While the algorithm still benefits from an initial manual alignment, its ability to then autonomously find an optimal coupling makes it a valuable tool for reducing the complexity of the experiment, making it easier and faster to operate.

CHAPTER 3

Implementation of a probe setup for Rydberg excitation

Having developed an automated system for fiber coupling in Chapter 2, this chapter turns to its application in the optical setup used for Rydberg excitation in the HQO experiment [27]. Stable fiber coupling is of particular importance for the probe arm of this setup, as the transmitted probe light is used to monitor whether the Rydberg transition has been driven successfully. However, before bringing the automated system into a test probe setup to simulate the actual experiment, it was necessary to characterize another new component of the setup, namely the achromatic lens which focuses the probe beam to its required beam waist which is currently planned to be around 17.5 µm in order to exceed the blockade radius of around 10 µm [7], as multiple Rydberg are to be performed.

The remainder of this chapter is structured as follows. Section 3.1 introduces the optical setup used for Rydberg excitation and describes the path of the probe beam through it. Section 3.2 presents the characterization of the probe beam, comparing three cameras for their suitability in beam waist measurements before determining the beam waist at the focus of the probe lens. Section 3.3 describes the combination of the characterized probe setup with the automated fiber coupling system developed in Chapter 2 and evaluates its performance in this more realistic configuration.

3.1 Optical setup for Rydberg excitation

In the HQO experiment, a well established [29] optical setup for Rydberg excitation is being used for the excitation of ^{87}Rb into a $n \gg 1$ Rydberg state. Fig. 3.1 depicts the setup, it consists of one arm with 480 nm light (control) and another with 780 nm light (probe), the lasers can be operated in a co- or counter-propagating manner.

For Rydberg excitation, the probe beam drives the $5S_{1/2} \rightarrow 5P_{3/2}$ transition using σ^+ polarized light while the control beam drives the Rydberg excitation from the intermediate $P_{3/2}$ state into the 85S Rydberg state using σ^- polarized light as shown in Fig. 3.2. The probe beam is in the single photon regime and the control laser at roughly 100 mW. As only the probe arm will be investigated in this chapter, the rest of this section will focus on it.

The setup is symmetric for both arms in order to be able to use light from both directions, but only the probe light can be read out without altering the setup as the probe light from one side is being guided

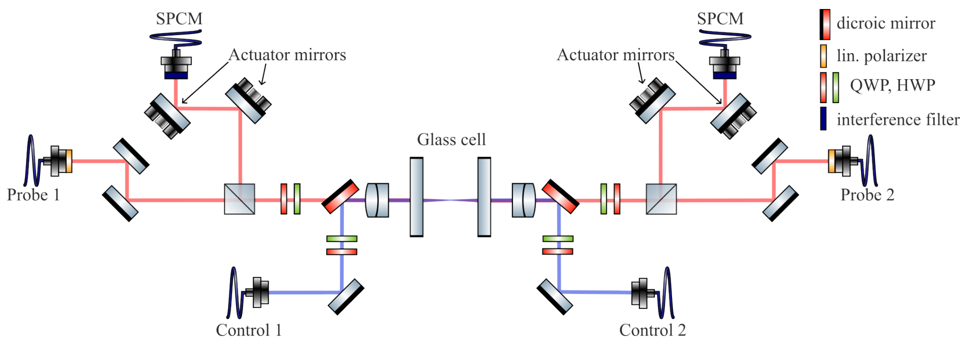

Figure 3.1: Sketch of the complete optical setup for Rydberg excitation using one lasers at 480 nm (control light) and another at 780 nm (probe light), which can be realised in either a co- or counter-propagating setup. When entering the setup the probe lights polarization is corrected using a linear polarizer before being circularly polarised with a half-wave plate (HWP) and quarter-wave plate (QWP). Its then focused to a beam waist of approximately 17.5 µm inside the glass cell and the transmitted light is afterwards collected by the single photon counter module (SPCM) on the other side. The control light enters the setup in a similar manner and is superimposed on the probe light by a dichroic mirror. It is planned to be focused to a beam waist of about 98 nm inside the glass cell. Image modified from [27].

into a single photon counter module (SPCM) on the other side and vice versa. The SPCM is described in more detail in Section 2.3.3. In the following, the path of the probe beam coming from the outcoupler labeled as Probe 1 in Fig. 3.1 will be described in more detail.

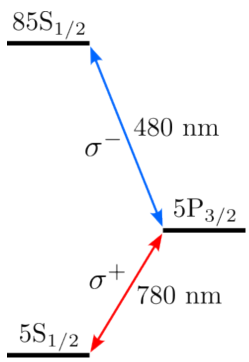

Figure 3.2: Level scheme of the three states involved in the Rydberg excitation of ^{87}Rb. A σ^+ polarized probe beam in the single photon regime drives the $5S_{1/2} \to 5P_{3/2}$ while a σ^- polarized control beam at roughly 100 mW drives the $5P_{3/2} \to 85S_{1/2}$. Image adapted from [30].

When entering the setup, the probe light is linearly polarized before being unalteredly transmitted through a polarizing beamsplitter (PBS). Through the combination of a half-wave plate (HWP) and quarter-wave plate (QWP) it is then circularly polarized to drive its required transition in the glass cell. Afterwards it passes through a dichroic mirror (only reflective for control beam) which alters its polarization but the wave plates are adjusted to compensate for this. The beam then passes through an achromatic lens with a focal length of $f = 175$ mm and is being focused to a beam waist of approximately 17.5 µm inside the glass cell, where it drives the transition to the intermediate state.

The transmitted probe light is collected by an identical achromatic lens and takes the same path as before until the PBS, where it is reflected towards the SPCM. The SPCM measures the amount of transmitted light in order to confirm whether the transition was driven. In order to keep the measured transmission independent from the coupling efficiency, the automated fiber coupling system has been developed to be able to easily correct this fiber coupling before taking measurements.

To check if the achromatic lens focuses the probe beam as intended a beam waist measurement was conducted in Section 3.2.2 and at this opportunity three cameras were examined and compared on their feasibility for beam waist measurements in Section 3.2.1. In order to test the previously developed automated fiber coupling system in combination with the probe lenses, a test setup for the probe beam was constructed in Section 3.3 and subsequently the collimation and coupling efficiency were investigated.

3.2 Characterization of the probe beam

To verify that the probe beam is focused as intended by the achromatic lens described in Section 3.1, a series of beam waist measurements was performed. Since accurately measuring the beam waist requires a camera that can resolve the intensity-profile of a Gaussian beam, three CMOS-cameras (CMOS: complementary metal-oxide-semiconductor) were compared and evaluated for this task. Building on this choice, Section 3.2.2 presents the actual beam waist measurement at the focus of the first lens, including an investigation of how the beam's position on the camera sensor affects the extracted beam waist.

3.2.1 Camera selection for beam waist measurements

Previous beam waist measurements in the HQO experiment were done using the Arducam MT9J001 with a software developed by S. Germer in his bachelor thesis [30] because of its small pixel size of 1.67 µm [31], which enables to resolve the intensity-profile of laser beams with small beam waists. Because the probe lens of the current setup is planned to have a larger beam waist than before with ~ 17.5 µm in order to exceed the blockade radius [7], it was possible to test the suitablility of other cameras for this beam waist measurement.

Table 3.1 shows some properties of the three CMOS-cameras that were compared. The pixel size is of course the most important property, but as it is the same for all cameras at 3.45 x 3.45µm none of them stands out in that regard. Another property all cameras share is that they are monochrome (denoted with MU), which is no problem as only the intensity of the laser light is of interest. The CS165MU/M has the smallest sensor size at 1/2.9", but this was not an issue as the beam was small enough to fit onto the sensor. This of course then also applied for the bigger sensors of the other cameras.

Model name	Pixel size / µm	Sensor size
Thorlabs LP126MU/M	3.45 x 3.45	1.1"
Thorlabs CS165MU/M	3.45 x 3.45	1/2.9"
Thorlabs CS505MU	3.45 x 3.45	2/3"

Table 3.1: Comparison of relevant specifications of three different CMOS-cameras [32][33][34].

Fig. 3.3 displays the setup used for comparing the detection of a collimated laser beam between the three cameras in Table 3.1. The camera was connected to a desktop computer via USB and the ThorImageCAM [35] software used to capture images. The laser had a wavelength of 780 nm.

Figure 3.3: Sketch of the setup used for comparing the detection of a collimated laser beam between the three cameras in Table 3.1. The beam approaches from the outcoupler on the right which was taken from the actual optical setup for Rydberg excitation 3.1 and therefore still has a linear polarizer installed.

The first camera to be investigated was the CS165MU/M, Fig. 3.4(a) shows an image of the collimated laser beam. As can be observed, the Gaussian intensity-profile is disturbed by a pattern of light and dark triangles. The theory for this is that this a combination of two different interference effects, one because of reflections at the protective glass pane in front of the sensor and one because of reflections within the sensor itself as it is made out of silicon, which is semi-transparent in the near-infrared [36].

Fig. 3.4(b) shows an image of the same beam captured with the CS165MU/M but without the protective glass in front of the sensor. The striped interference pattern is what is assumed to be caused by the internal reflections in the sensor, while the circular stripes which are now more visible could be caused by a dust particle on one of the optical components. Before investigating how this impacts the intensity-profile of a focused beam, it was first checked if the other cameras have the same issue.

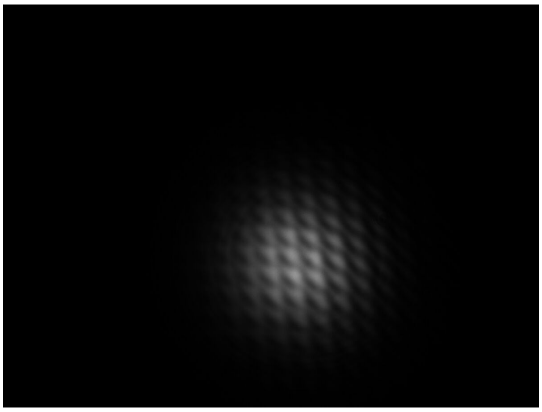

(a)

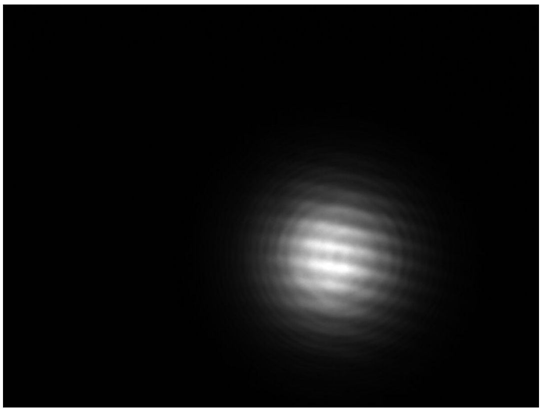

(b)

Figure 3.4: Image of the collimated probe laser beam taken with the Thorlabs CS165MU/M camera. **(a)** Due to reflections at the glass pane protecting the sensor and within the silicon sensor itself a pattern of light and dark triangles can be observed. **(b)** After removing the glass pane, only the interference due to the reflections in the sensor can be observed.

Fig. 3.5(a) shows an image of the collimated beam captured with the CS505MU, whose protective glass pane had already been removed. It also shows an interference pattern and fringes caused by dust particles. The distance between the minima and maxima of the interference pattern is smaller compared to Fig. 3.4(b) and in some spots the pattern is blurred.

The image taken with the LP126MU/M in Fig. 3.5(b) again shows a more complex pattern as the camera still had its protective glass pane on.

As all cameras showed similar effects when illuminated, only the CS165MU/M was further used to

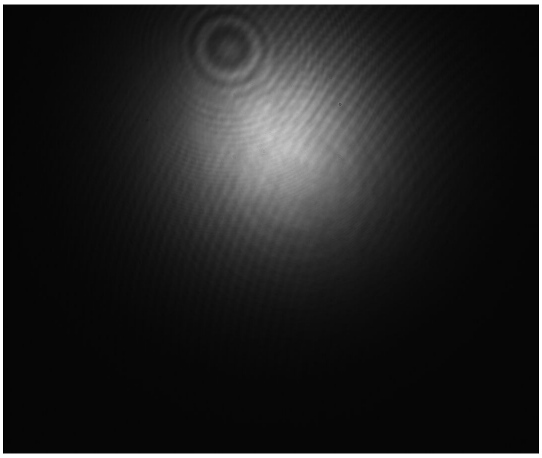

(a)

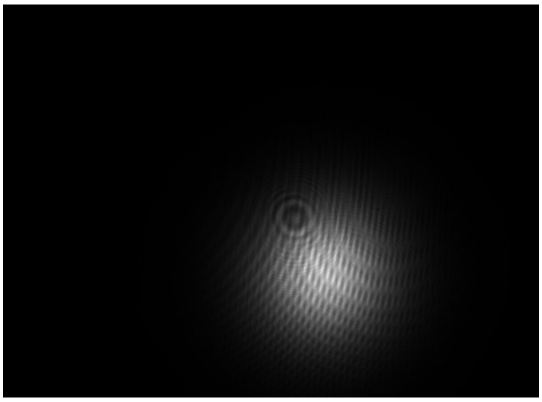

(b)

Figure 3.5: Image of the collimated probe laser beam taken with two different cameras. **(a)** Image taken with the Thorlabs CS505MU. Its protective glass pane was already removed, hence only the interference due to reflections within the senor is observed. **(b)** Image taken with the Thorlabs LP126MU/M. It still had its protective glass pane on and is therefore also showing a pattern of overlapping interferences.

observe how well it can capture the intensity-profile of a focused beam as it was the easiest to setup due to its small size.

3.2.2 Beam waist of the focussing lens

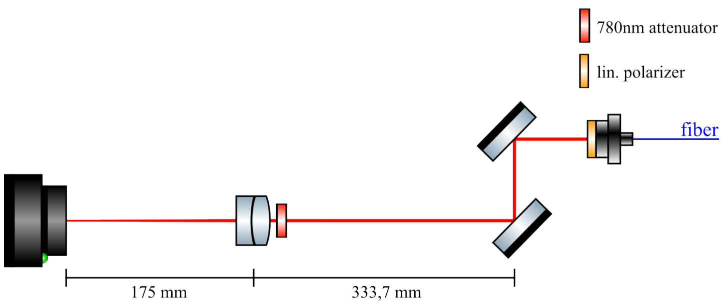

Figure 3.6: Sketch of the setup used for measuring the beam waist of the focused beam. The beam approaches from the outcoupler on the right which was taken from the actual optical setup for Rydberg excitation 3.1 and therefore still has a linear polarizer installed. It is then steered by two mirrors through the achromatic probe lens onto the CS165MU/M camera, which is placed at the focal point of the lens. A neutral density filter in front of the lens attenuates the beam in order to not saturate the camera.

Having decided on a camera, the next step was to see if the interference pattern observed in Section 3.2.1 impacts the intensity-profile of the focused beam. For this the achromatic probe lens was introduced into the setup as depicted in Fig. 3.6, with a distance of 333.7 mm between the lens and the second mirror after the outcoupler as this will be their distance in the actual setup. A neutral density filter with an experimentally found OD of 3.59 was placed in front of the lens, as the power of the focused beam would otherwise saturate the camera. The camera was placed at the focal point of the probe lens, at distance of 175 mm to the probe lens.

As can be seen in Fig. 3.7(a) it was possible to capture the Gaussian intensity-profile of the beam without any visible disturbances. To find the beam waist, a Gaussian function of the form [30]

$$f(x) = A \cdot e^{-2(x-x_0)^2/w_0^2}, \tag{3.1}$$

with A being the amplitude, x_0 the position of the curves maximum and w_0 the beam waist, was fitted to the image data in two dimensions, resulting in the plot in Fig. 3.7(b). The plots data points show the measured intensity of two pixel rows which intercept the center of the intensity-profile, one vertically and the other horizontally. The curves show the fitted Gaussian functions to the respective data points and below the plot the residuals of the fits are shown.

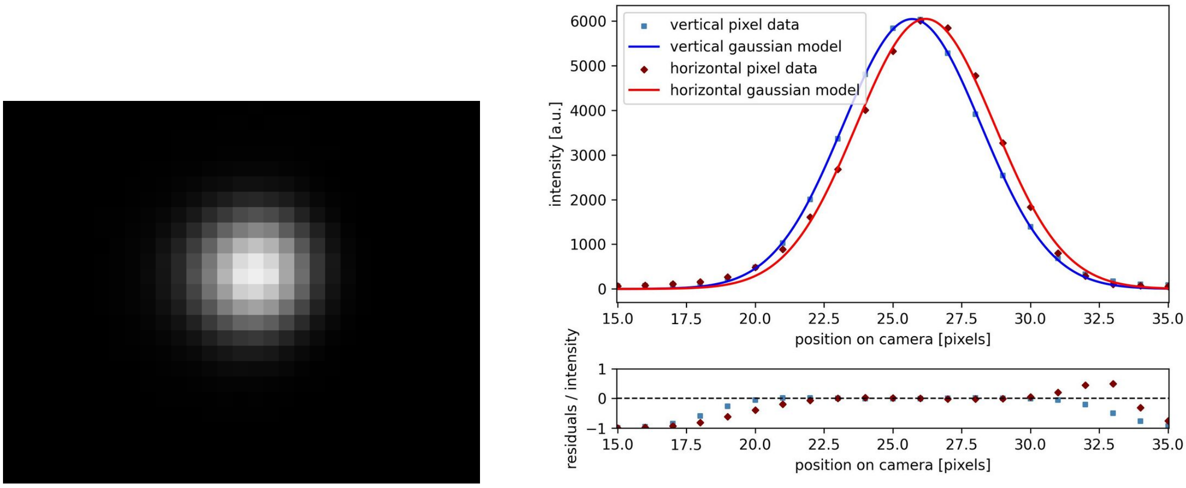

(a) (b)

Figure 3.7: **(a)** Image of the focused laser beam at the focal point of the probe lens. **(b)** 2D Gaussian fit as per Eq. 3.1 of the focused beam image with residuals to determine the beam waists in horizontal and vertical direction. The resulting beam waists are given in Eq. 3.2.

Both curves trace their respective data points well, with residuals especially around the peak being almost zero. From the fits one can extract the horizontal and vertical beam waist:

$$w_0^{\text{vertical}} = (17.31 \pm 0.11)\,\mu\text{m} \tag{3.2}$$

$$w_0^{\text{horizontal}} = (17.35 \pm 0.16)\,\mu\text{m} \tag{3.3}$$

The values agree within their error range and are close to the wanted beam waist of 17.5 µm. The given errors are only those of the Gaussian fit and as the camera was only placed roughly at the focal point, the beam waist values can definitely get lower. As it has been shown that it is possible to use the CS165MU/M to perform beam waist measurements, a translation stage will be used in the following to firstly see how the horizontal position of the beam on the camera sensor affects the measurement and secondly to obtain the minimum beam waist by moving the camera along the optical axis around the focus point.

The horizontal position of the laser beam on the camera sensor is presumed to be a major error source because of the interference pattern observed in Section 3.2.1. To investigate how this affects the resulting beam waist, the camera was mounted onto a linear translation stage and moved in 100 µmeter steps perpendicular to the optical axes, taking an image after every step. Afterwards a Gaussian fit was applied to every image in vertical and horizontal direction and the resulting beam waists were plotted against their respective translation stage position (see Fig. 3.8).

In the figure, one can see that the camera position heavily influences the resulting beam waists, with a difference of up to 2 µm (~ 10 %) between the horizontal beam waists and up to 1 µm (~ 5 %) between the vertical ones. The camera had to be placed a bit off from the focal point of the lens in order to fit the translation stage, hence the overall larger beam waists than before. Although no pattern is visible that would point to an influence of the interference pattern observed in Sec. 3.2.1, the values are generally lower for one half of the sensor than the other, with the center being at a translation stage position of about 13.8 mm. The reason for this is unknown, but it could be attributed to a difference of the sensors sensitivity or an intensity drift of the laser.

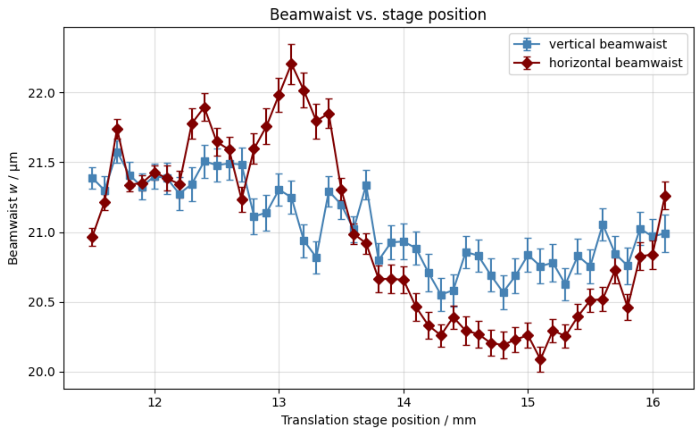

Figure 3.8: As per Eq. 3.1 obtained beam waists in horizontal and vertical direction at different camera positions after horizontal translation in 100 µm steps of the camera. A difference of up to 2 µm (~ 10 %) between the horizontal beam waists and up to 1 µm (~ 5 %) between the vertical ones can be noticed.

Some of the general fluctuations of the beam waists could be attributed to the number of pixels which are illuminated by the beam. Fig. 3.9 shows an example of this: depending on whether the beam center hits the center of a pixel or the edge between two pixels, the apparent beam shape recorded by the pixels drastically changes. This effect of course levels out the bigger the beam gets, but for example in Fig. 3.8 one pixel is ~ 10 % the size of the beam waist and could therefore accommodate for some of the beam waist differences.

Despite the aforementioned issues, the measurement of the minimum beam waist was conducted next. For this, the same translation stage as used for the above measurements was rotated by 90° to be able to move the camera along the optical axis. Then the analogous process as for the horizontal movement measurements was performed. The resulting plot is depicted in Fig. 3.10 and shows what one would expect: a minimum beam waist at the lenses focal point and a symmetrical increase of the measured beam waist in both directions as the camera is moved away from the focal point. One can observe a

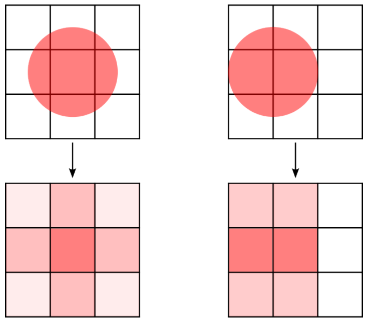

Figure 3.9: Depiction of how the way a beam hits an array of camera pixels (top) can change the number and intensity of illuminated pixels and therefore the apparent beam shape (bottom).

slight astigmatism (difference in vertical and horizontal focal point position) which is probably caused by an imperfect positioning of the probe lens.

The from Fig. 3.10 resulting horizontal and vertical beam waists of the probe lens are:

$$w_0^{\text{vertical}} = (16.90 \pm 0.03)\,\mu\text{m} \tag{3.4}$$

$$w_0^{\text{horizontal}} = (16.80 \pm 0.01)\,\mu\text{m} \tag{3.5}$$

These values only differ by 0.1 µm or 0.6 % and are 0.6 µm and 0.7 µm respectively smaller than the target beam waist of ∼ 17.5 µm. But again, the given errors are only those of the Gaussian fit, so on the basis of the previous measurements an additional error of 5-10% has to be assumed because of the beam waists dependence on the beam position on the camera sensor. In a worst case scenario with an error of 10 % this would result in an error of about 1.7 µm for the beam waist in both directions. Even with this deviation, the beam waists are acceptable for the experiment.

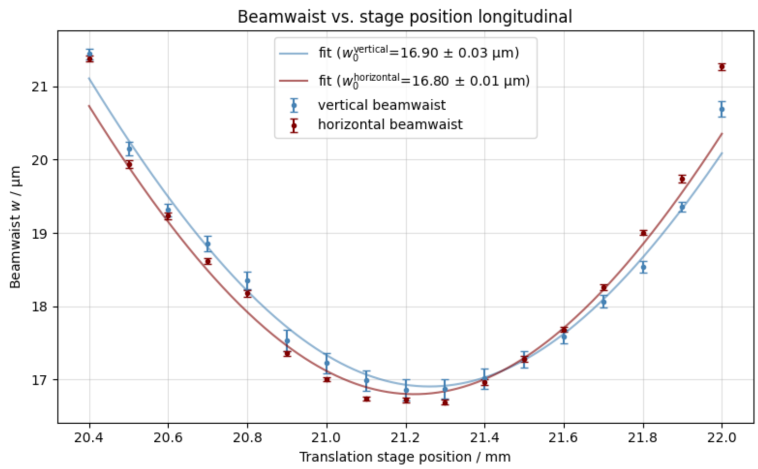

Figure 3.10: Beam waists at different camera positions after translation of the camera along the optical axis. A Gaussian function was fitted to the beam waists in vertical and horizontal direction in order to obtain the beam waists in each direction at the focal point of the focussing lens. These are given in Eq. 3.4.

3.3 Testing the automatic fiber coupling optimization in the complete probe setup

After developing an automated fiber coupling system and characterizing the achromatic lens of the optical probe setup, this section deals with the combination of the two components in order to simulate the probe arm (780 nm light) of the optical setup for Rydberg excitation of the HQO experiment. Fig. 3.11 shows the complete test probe setup, the wiring of the actuator mirror mounts is same as in Fig. 2.5 as the power meter had to be used again for feedback on the transmitted power.

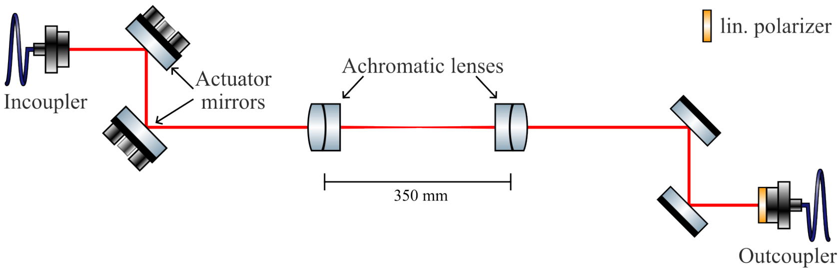

Figure 3.11: Sketch of the test setup used for simulating the probe arm of Fig. 3.1. The 780 nm light entering the setup from the right is focused to a beam waist of approximately 17.5 µm and after being recollimated again is steered by two actuated mirrors into an incoupler.

As described in Sec. 3.2.2, the first achromatic lens with a focal length of $f = 175$ mm focuses the probe light to a beam waist of about 17.5 µm. The second achromatic lens is identical to the first one and placed at $2f$ to recollimate the probe light. Fig. 3.12 shows an image of a shear plate interferometer placed into the beam path after the second achromatic lens in order to check the collimation of the beam. In the image, the second achromatic lens has already been adjusted so that the red stripes, which occur because of interference of the beam with itself inside the interferometer, are parallel to the optical axis of the probe beam. Before adjusting, the red stripes were tilted in regards to the optical axis.

Figure 3.12: Examination of the beam collimation after the second achromatic lens with a shear plate interferometer. The alignment of the red stripes inside the interferometer parallel to the optical axis confirms that the beam is collimated again after being decollimated by the first achromatic lens of the setup in Fig. 3.11.

As the incoupler and the mirror mounts with actuators were newly installed into this setup, meaning the fiber coupling into the incoupler had not been done before for this system, it was tested if the optimization algorithm introduced in Section 2.3 would firstly be able to find any signal, which can be quite hard with an already installed incoupler lens as the focused beam has the same size as the fiber core, and secondly if it would be able to reach a high coupling efficiency.

The algorithm failed at the first task of finding any kind of signal, but it has to be noted that it was not possible to find a signal by hand until adjusting the incoupler itself which the optimization cannot do as it can only control the mirror mounts with actuators. But it was to be expected that the model based approach of the optimization algorithm would have a hard time without any feedback signal, so a small Python script was created which uses a more systematic approach by scanning a definable area in either a grid or spiral pattern, subsequently called the signal finder. The patterns are depicted in Fig. 3.13.

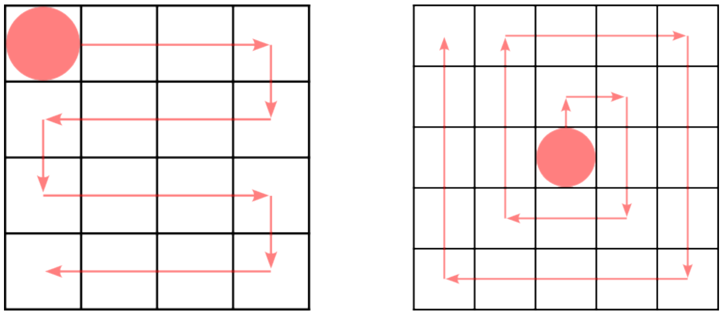

Figure 3.13: Sketch of the two search patterns of the signal finder script used for establishing an initial fiber coupling. The red circle represents the laser beam, while each square represents a position on the surface of the fiber where the beam is moved to and a power measurement is done in order to check if light has been transmitted through the fiber.

As the name suggests, using the grid pattern the signal finder moves the beam across the fiber surface in serpentine movements in a grid pattern and measures the transmitted power until a definable power threshold is reached, at which point the signal finder stops. Using the spiral pattern the signal finder moves the beam in circles around its starting point, with the radius of each circle growing after completing the one before until a maximum radius has been reached. For both patterns, only one mirror was moved at first and if the power threshold was not reached the other mirror was moved in the same pattern until the signal finder stops.

Using the signal finder with a spiral pattern, it was possible to achieve a transmitted power of 35 µW out of the 1 mW of power before the incoupler. It was then tried to improve the coupling via the optimization algorithm and a transmitted power of 170 µW was reached, which is an improvement but only equals a coupling efficiency of 17 %. After further improvement by hand a coupling efficiency of 30 % was reached but could not be exceeded anymore. The low maximum coupling efficiency could be attributed to the fact that the shear plate interferometer only gives a rough estimation of the beams collimation while the rather poor performance of the optimization algorithm could be attributed to the differing requirements on the mirror movement for performing a new coupling rather than a recoupling.

CHAPTER 4

Conclusion and Outlook

In this thesis, an automated fiber coupling system for the HQO experiment setup was developed and an optical setup for Rydberg excitation of ^{87}Rb was characterized.

In Chapter 2, the PiezoMike linear actuators were characterized, based on measurements previously done by E. Huland. Through iterative adjustment of the backward step sizes of each actuator the discrepancy between the movement directions could be minimized to ensure reliable and reproducible control of the actuators. Based on this, the automated fiber coupling system was developed and tested using the machine-learning optimization package M-LOOP. The system was able to reach a coupling efficiency of $\sim$ 80 % using a power meter as feedback and was also successful at optimizing the count rate when using a SPCM as feedback although no coupling efficiency can be given as the count rate before the SPCM could not be measured. Optimization on average took 1-2 minutes with small readjustments being even faster.

In Chapter 3 the optical setup for Rydberg setup was explained and a characterization of the probe beam was conducted. After comparing three CMOS-cameras, the CS165MU/M was further used for measuring the beam waist of the probe beam. The measured beam waists at the focal point of the achromatic lens were measured as $w_0^{\text{vertical}} = (16.90 \pm 0.03)$ µm and $w_0^{\text{horizontal}} = (16.80 \pm 0.01)$ µm. The deviations from the aimed for value of $\sim$ 17.5 µm are acceptable, even considering the expected additional error of up to 10 % caused by the dependence of the beams position on the camera sensor, resulting in an error of 17 µm in both directions. Last of all, the automated fiber coupling system was installed in a test probe setup. As the system failed at establishing a fiber coupling of the newly built setup, an additional algorithm was developed and used which systematically scans an area in either a grid or spiral pattern in order to obtain a first signal. The low coupling efficiency of $\sim$ 30 % reached through a combination of automated optimization and manual alignment at the end was attributed to poor collimation of the beam.

Altogether, it was possible to develop an automated fiber coupling system for the fast and reliable realignment of a critical coupling in the HQO experiment.

The next step would be to precisely align the test probe setup to improve the collimation and check what coupling efficiency can be reached. Afterwards, the actuator mirror mounts as well as the achromatic lenses need to be introduced into the actual experiment setup and an experiment sequence for the automated optimization has to be added. Further into the future, the automated fiber coupling system could be introduced to other parts of the experiment or to other experiments.

APPENDIX **A**

Appendix

Optimization algorithm parameters

This list gives a brief overview on the parameters seen in Fig. 2.11(b) & 2.13(b) which could be adjusted in order to influence the performance of the optimization algorithm introduced in Section 2.3.1:

- Algorithm: selection of the algorithm to be used by M-LOOP to model the experiment. This was always set to 'neural_net'.
- settle_time: time given in seconds which the script paused before taking a power/count rate measurement in order to wait for the mirrors to settle into their new position. 0.15 s was experimentally found to be the lowest value without losing measurement accuracy.
- max_dist_µm: the maximum distance D for position values to be proposed by the script. 3 µm was sufficient for most scenarios, except sometimes when starting with a very low coupling efficiency $< 1\,\%$.
- num_of_axes: number of actuators to be used for the optimization. Was always set to 4 except for the very first tests of the script.
- target_power: when the predicted power by the model exceeds this value, the optimization ends. Has to be manually set depending on the laser power one is working with.
- max_runs: maximum number of runs after which the optimization stops if no other termination condition is satisfied. Was set to 100 for the most part.
- max_runs_no_improvement: the optimization stops if no higher power prediction was made since this amount of runs. Was set to 20 for the most part.
- trust_region: the proposed positions are confined to an area of this value multiplied with max_dist_µm around the current best power position. Was set to 0.5 for the most part.
- initial_random_runs: supposedly the algorithm first proposes this number of random positions within max_dist_µm in order to acquire information about the cost landscape. It was observed that the algorithm often started to propose optimized positions earlier than that, the reason for this was not investigated. Was set to 10 for the most part.

Bibliography

[1] V. Montenegro et al., *Review: Quantum Metrology and Sensing with Many-Body Systems*, Physics Reports **1134** (2025) 1, URL: https://www.sciencedirect.com/science/article/pii/S0370157325001565?via%3Dihub (cit. on p. 1).

[2] S. Pirandola et al., *Advances in quantum cryptography*, Adv. Opt. Photon. **12** (2020) 1012, URL: https://opg.optica.org/aop/abstract.cfm?uri=aop-12-4-1012 (cit. on p. 1).

[3] J. Gambetta, J. Chow and M. Steffen, *Building logical qubits in a superconducting quantum computing system*, npj Quantum Information **3** (2017) 2, URL: https://www.nature.com/articles/s41534-016-0004-0 (cit. on p. 1).

[4] G. Kurizki et al., *Quantum technologies with hybrid systems*, Proceedings of the National Academy of Sciences **112** (2015) 3866, URL: https://www.pnas.org/doi/full/10.1073/pnas.1419326112 (cit. on p. 1).

[5] C. Wind et al., *Entanglement of mechanical oscillators mediated by a Rydberg tweezer chain*, Phys. Rev. A **113** (2026) 053705, URL: https://journals.aps.org/pra/abstract/10.1103/qqf3-wx7m (cit. on p. 1).

[6] C. Wind, *Experimental setup for a Rydberg atom–mechanical oscillator hybrid system*, PhD Thesis: University of Bonn, 2026 (cit. on p. 1).

[7] E. Urban et al., *Observation of Rydberg blockade between two atoms*, Nature Physics **5** (2009) 110, URL: https://www.nature.com/articles/nphys1178 (cit. on pp. 1, 18, 20).

[8] M. Fleischhauer, A. Imamoglu and J. P. Marangos, *Electromagnetically induced transparency: Optics in coherent media*, Review of Modern Physics **77** (2005) 633, URL: https://journals.aps.org/rmp/abstract/10.1103/RevModPhys.77.633 (cit. on p. 1).

[9] S. H. Autler and C. H. Townes, *Stark Effect in Rapidly Varying Fields*, Phys. Rev. **100** (1955) 703, URL: https://journals.aps.org/pr/abstract/10.1103/PhysRev.100.703 (cit. on p. 1).

[10] H. Zhang et al., *Fast automatic fiber coupling using global optimization algorithms approaching the experimental efficiency limit*, Review of Scientific Instruments **97** (2026) 023001, URL: https://pubs.aip.org/aip/rsi/article/97/2/023001/3379008/Fast-automatic-fiber-coupling-using-global (cit. on p. 1).

[11] P. B. Wigley, P. J. Everitt, A. van den Hengel et al., *Fast machine-learning online optimization of ultra-cold-atom experiments*, Scientific Reports **6** (2016) 25890, URL: https://www.nature.com/articles/srep25890 (cit. on pp. 1, 11).

[12] D. Meschede, *Optik, Licht and Laser*, 3rd ed., Vieweg+Teubner, 2008 (cit. on pp. 3, 5).

[13] V. S. Vel, *Automated Fiber Coupling with Actuated Mirrors*, Masters Thesis: Massachusetts Institute of Technology, 2025 (cit. on p. 4).

[14] E. Huland, *Precise optical trap alignment using piezo-motorized mirrors*, Bachelor Thesis: University of Bonn, 2026 (cit. on pp. 4, 5, 7).

[15] *Thorlabs P3-780PM-FC-10 datasheet*, URL: https://media.thorlabs.com/globalassets/items/p/p3/p3-/p3-780pm-fc-10/ttn005539-e0w.pdf?v=0116015000 (visited on 05/08/2026) (cit. on p. 5).

[16] *PiezoMike Linear Actuators*, URL: https://www.physikinstrumente.com/en/expertise/technology/piezoelectric-drives/piezomike-linear-motors (visited on 13/07/2026) (cit. on pp. 5, 6).

[17] *Rubidium Rydberg Nonlinear Quantum Optics website*, URL: https://www.iap.uni-bonn.de/nqo/en/research/rubidium-rydberg-nqo (visited on 31/07/2026) (cit. on p. 5).

[18] *PiezoMike Linear Actuators controller*, URL: https://www.pi-usa.us/fileadmin/user_upload/pi_us/files/product_datasheets/E870_Stick_Slip_Piezo_Motor_Controller.pdf (visited on 31/07/2026) (cit. on p. 6).

[19] *PIPython package*, URL: https://pypi.org/project/PIPython/ (visited on 31/07/2026) (cit. on p. 6).

[20] *PiezoMike Linear Actuators datasheet*, URL: https://www.physikinstrumente.com/fileadmin/user_upload/physik_instrumente/files/datasheets/N-470-Datasheet.pdf (visited on 31/07/2026) (cit. on p. 6).

[21] *Thorlabs PM100USB datasheet*, URL: https://media.thorlabs.com/globalassets/items/p/pm/pm1/pm100usb/19570-d02.pdf?v=0116021234 (visited on 05/08/2026) (cit. on pp. 7, 8).

[22] L. P. Kaelbling, M. L. Littman and A. W. Moore, *Reinforcement Learning: A Survey*, Journal of Artificial Intelligence Research **4** (1996) 237, URL: https://www.jair.org/index.php/jair/article/view/10166 (cit. on p. 11).

[23] P. I. Frazier, *Taking the Human Out of the Loop: A Review of Bayesian Optimization*, Institute of Electrical and Electronics Engineers **104** (2016) 148, URL: https://ieeexplore.ieee.org/document/7352306 (cit. on p. 11).

[24] M. A. Nielsen, *Neural Networks and Deep Learning*, Determination Press, 2015 (cit. on pp. 11, 12).

[25] *M-LOOP Neural Net model source code*, URL: https://github.com/michaelhush/M-LOOP/blob/master/mloop/neuralnet.py (visited on 06/08/2026) (cit. on p. 12).

[26] *Single Photon Counting Module COUNT®-Series*, URL: https://www.lasercomponents.com/fileadmin/user_upload/home/Datasheets/lc-photon-counter/count-series.pdf (visited on 01/08/2026) (cit. on pp. 15, 16).

[27] J. Gamper, *Atom Preparation and Rydberg Excitation of Rubidium Atoms*, Masters Thesis: University of Bonn, 2024 (cit. on pp. 15, 18, 19).

[28] A. Özcagi, *Setup and Characterization of Single-Photon Counters for Optical Correlation Measurements*, Bachelor Thesis: University of Bonn, 2026 (cit. on p. 16).

[29] H. Gorniaczyk, C. Tresp, J. Schmidt, H. Fedder and S. Hofferberth, *Single-Photon Transistor Mediated by Interstate Rydberg Interactions*, Phys. Rev. Lett. **113** (2014) 053601, URL: https://journals.aps.org/prl/abstract/10.1103/PhysRevLett.113.053601 (cit. on p. 18).

[30] S. Germer, *Frequency stabilization of a laser and a high resolution optical setup for excitation of ultracold Rydberg atoms*, Bachelor Thesis: University of Bonn, 2023 (cit. on pp. 19, 20, 23).

[31] *Arducam MT9J001 datasheet*, URL: https://blog.arducam.com/downloads/modules/industrial/1Inch2.3_10_Megapixel_MT9J001_CMOS_Camera_Module_DS.pdf (visited on 02/08/2026) (cit. on p. 20).

[32] *Thorlabs LP126MU/M datasheet*, URL: https://media.thorlabs.com/globalassets/items/l/lp/lp1/lp126cu_m/itn005664-d02.pdf?v=0116125500 (visited on 02/08/2026) (cit. on p. 20).

[33] *Thorlabs CS165MU/M datasheet*, URL: https://media.thorlabs.com/globalassets/items/c/cs/cs1/cs165mu1/itn004347-d02.pdf?v=0116110511 (visited on 02/08/2026) (cit. on p. 20).

[34] *Thorlabs CS505MU datasheet*, URL: https://media.thorlabs.com/globalassets/items/c/cs/cs2/cs2100m-usb/itn002518-d02.pdf?v=0116110538 (visited on 02/08/2026) (cit. on p. 20).

[35] *ThorImageCAM software*, URL: https://www.thorlabs.com/software-pages/ThorCam (visited on 02/08/2026) (cit. on p. 20).

[36] *Teledyne Visions Solutions - Etaloning in the NIR*, URL: https://www.teledynevisionsolutions.com/de-de/learn/learning-center/imaging-fundamentals/excelon-technology--novel-performance-enhancing-ccd-technology/ (visited on 03/08/2026) (cit. on p. 21).